

www.acsami.org Research Article

Surface-Based Post-synthesis Manipulation of Point Defects in Metal Oxides Using Liquid Water

Heonjae Jeong, Elif Ertekin, and Edmund G. Seebauer*



Cite This: ACS Appl. Mater. Interfaces 2022, 14, 34059-34068



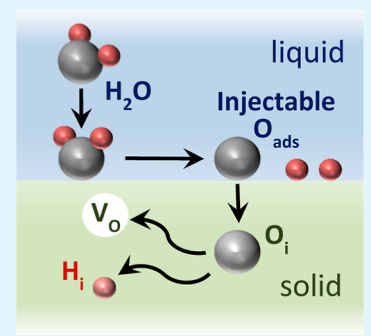
ACCESS

III Metrics & More

Article Recommendations

SI Supporting Information

ABSTRACT: Initial synthesis of semiconducting oxides leaves behind poorly controlled concentrations of unwanted atomic-scale defects that influence numerous electrical, optical, and reactivity properties. We have discovered through self-diffusion measurements and first-principles computations that poison-free oxide surfaces inject interstitial oxygen atoms into the crystalline solid when simply contacted with liquid water near room temperature. These interstitials diffuse quickly to depths of 20 nm $-2~\mu m$ and are likely to eliminate prominent classes of unwanted defects or neutralize their action. The mild conditions of operation access a regime for oxide fabrication that relaxes important thermodynamic constraints that hamper defect regulation by conventional methods at higher temperatures. The surface-based approach appears well-suited for use with nanoparticles, porous oxides, and thin films for applications in advanced electronics, renewable energy storage, photocatalysis, and photoelectrochemistry.



KEYWORDS: defects, oxygen, interstitials, vacancies, metal oxides, ZnO, TiO2, Ga2O3

■ INTRODUCTION

The lessened chemical coordination present at solid surfaces compared to that in the bulk facilitates the creation and destruction^{1,2} of point defects such as interstitial atoms. Metal oxides such as ZnO and TiO2 are examples wherein clean^{3,4} surfaces create interstitials of oxygen $(O_i)^{5-7}$ or the metal cation $(M_i)^{8-10}$ from the corresponding adsorbed atoms with energy barriers below roughly 1 eV. The atomic configurations for interstitial injection resemble those for site hopping in the bulk, with barriers only slightly higher.⁶ The modest hopping barriers of O_i (Supporting Information Tables S1 and S2) and M_i¹¹ in oxides, coupled with those for injection, should enable clean surfaces to populate the nearby bulk with interstitials even near room temperature, as hinted recently for UO₂. 12 Such surprisingly low temperatures access a regime wherein equilibrium concentrations of native defects become vanishingly small, and kinetic rather than thermodynamic effects dominate the defect behavior. Hyperdoping of silicon above the solubility limit illustrates the benefits of kinetic dominance,13 although the possibilities for wielding such kinetic tools for defect manipulation near room temperature have not been recognized.

For O_i injection into oxides, post-synthesis elimination of unwanted defects becomes possible, or compensation of their action as donors or acceptors. Realizing these possibilities requires generating injectable adsorbates, however. O_2 gas dissociation into adsorbed O often requires temperatures above 500 °C, 5,6 for example. By contrast, many oxides are known to dissociate H_2O at room temperature. Published studies $^{15-17}$ show consistently that dissociation proceeds only partially, with the most stable adsorbed products being H and

OH. However, experimental studies have usually employed a vacuum environment or have used methods that would struggle to detect adsorbed O as a minor product. First-principles computations have focused on the most stable products or have not included explicit adsorbate—solvent interactions that could produce adsorbed O as a secondary product. Thus, complete water dissociation remains a possibility. Even as a side reaction, realization of this possibility with suitably cleaned oxides would enable access to the low temperature regime by simple immersion in water. Shifting the fluid phase from gas to liquid would simplify material fabrication and enable possible rate enhancements due to pH or electrochemical potentials.

Here, we show by isotopic self-diffusion measurements combined with first-principles calculations using the density functional theory (DFT) that poison-free oxide surfaces do indeed inject O_i when contacted with liquid water near room temperature. For single-crystal oxides of zinc, titanium, and gallium, O_i penetrates to depths ranging between 20 nm and 2 μ m. This O_i almost certainly eliminates oxygen vacancies (V_O) within the penetration depth and may form complexes with hydrogen interstitials (H_i) that neutralize their action as adventitious donors. The results point the way toward broad applications in nanostructures, thin films, and porous materials.

Received: April 30, 2022 Accepted: July 6, 2022 Published: July 18, 2022





METHODS

Experiments. We employed isotopic self-diffusion experiments to monitor defect behavior indirectly. 18 The oxide is exposed to a fluid containing isotopically labeled O that enters the solid and undergoes defect-mediated diffusion. In our work, ubiquitous adsorbates that poison Oi injection were first removed, followed by exposing singlecrystal metal oxide specimens to liquid H₂¹⁸O at 30-80 °C. Depth profiles of 18O were measured afterward by secondary ion mass spectrometry (SIMS).

Specimen Preparation. All ZnO, TiO2, and Ga2O3 specimens were single crystals and polished on one side. Undoped wurtzite ZnO (GmbH) was cut to 5–10 mm \times 5 mm \times 0.5 mm. Undoped rutile $TiO_2(110)$ (MTI Corp.) was cut to 5–10 mm × 5 mm × 0.5 mm. β -Ga₂O₃(201) (Novel Crystal Technology, Inc.) with Sn doping at 1.4 \times 10¹⁸ cm⁻³ was cut to 10 mm \times 5 mm \times 0.65 mm. Atomic force microscopy indicated that all oxides had a surface roughness of <5 Å.

To remove surface poisons that inhibit O_i creation, ^{3,4} some specimens of ZnO(0001) and TiO₂(110) were treated with liquid solutions. For ZnO, the procedure employed 10% hydrogen peroxide for 20 min at 80 °C. For TiO2, the procedure employed a solution of 30% NH₄OH and H₂O mixed in a 1:2 ratio for 40 min at 25 °C.

All other specimens (including Ga₂O₃, for which a liquid treatment has not yet been optimized) underwent high-temperature annealing in low-pressure natural-abundance O_2 gas (99.995%) for 4 h in an ultrahigh vacuum (UHV)-compatible apparatus described elsewhere.³ These specimens were first degreased by successive 10 min ultrasonic baths in reagent-grade acetone, isopropanol, ethanol, and methanol. Annealing followed, with the pressures of O₂ and temperatures being 1×10^{-5} Torr and 500 °C for ZnO, 5×10^{-6} Torr and 450 °C for TiO_2 , and 1 × 10⁻⁴ Torr and 550 °C for Ga_2O_3 , respectively. For ZnO and TiO2, wherever direct comparisons between the two procedures were possible, the vacuum and wet etching approaches yielded similar values for the net injection flux F and mean diffusion length λ , including the temperature dependences.

Isotopic Self-Diffusion and Profile Measurement. Isotopic self-diffusion using liquid water employed a custom-designed apparatus wherein single crystals were immersed in 5 mL of ¹⁸Olabeled water H₂¹⁸O (10 atomic % ¹⁸O, Sigma-Aldrich) at temperatures ranging between 30 and 80 °C for 1 h in a laboratory air environment. The incorporated ¹⁸O concentration profiles were measured by ex situ time-of-flight secondary ion mass spectrometry (TOF-SIMS, PHI-TRIFT III instrument) employing a Cs ion beam source operating at 3 keV, with baseline concentrations checked against known isotopic fractions. In many cases, multiple profiles were measured at up to three different places on a specimen's surface.

Profile metrics were obtained using an analytical mesoscale approach based upon profile-by-profile determination of the slopes and intercepts in semi-logarithmic plots. 19 The approach employs coupled partial differential equations to describe the time evolution of the mobile and stationary forms of the isotopic label. Few assumptions are made about the kinetic mechanisms at play except that the diffusion of the label occurs via a rapidly mobile intermediate (such as O_i) that is permanently sequestered by a single trapping event. For an open system where a new label enters the solid at the surface, solution of the differential equations yields profiles having exponential shapes at short times whose details depend upon parameters representing composites of elementary-step rate constants. Profiles are fitted by

$$\ln\left(\frac{C - C_0}{C_0^{\mathrm{T}} - C_0}\right) = \ln\left(\frac{F}{\lambda [C_0^T - C_0]}t\right) - \frac{x}{\lambda}$$
(1)

where C is the measured concentration of $^{18}\mathrm{O}$, C_0 is the natural abundance concentration of 18 O, C_0^T denotes the total concentration of the lattice sites capable of exchanging with O_i , t is the diffusion time, and x is the spatial coordinate with x = 0 referring to the surface. The profile slope yields λ , while the intercept yields F. These two composite parameters yield a third useful profile metric, the effective diffusivity $D_{\rm eff}$.

The model assumes that only one sequestration event occurs for each Oi during the experiment. The validity of this assumption depends upon whether or not the principal sequestration site can be saturated (e.g., a vacancy vs a dislocation) and the concentration of such sites. However, the values of F obtained by this model match within the experimental error the values obtained independently by integrating the areas under the profiles and assuming a constant flux. The parameter λ retains utility as a phenomenological profile metric regardless of physical interpretation.

Oi has appreciable mobility even at room temperature. This mobility, together with the stability of diffused profiles toward longterm storage near 25 °C, indicates that any O_i present after the injection ends soon disappears by bulk trapping or diffusion back to the surface.

Because the water was only 10% isotopically pure in ¹⁸O, computation of the net injection flux F included a factor of 10 to represent the total injected flux of both isotopes. $D_{
m eff}$ is a phenomenological parameter that does not equal the tracer diffusivity (as it does in prior gas exchange experiments⁵) because at these low temperatures, the solids are far from equilibrium.

For Ga₂O₃, we applied the analysis at depths below about 20 nm. The deviations from linearity shallower than 20 nm could result from near-surface band bending and its associated electric field, which exerts a drift force on the (-2) charged interstitials that can lead to pile-up. ²⁰ The clean surface of β -Ga₂O₃($\overline{2}$ 01) in vacuum exhibits band bending that varies considerably with treatment protocols but has been measured at 0.26 eV,²¹ which leads to a space-charge width of about 7 nm that is broadly consistent with this picture. Such effects do not affect determination of F or λ deeper in the bulk.

Computations Using DFT. Model for the Oxide Solids and Their Surfaces. DFT calculations employed the Vienna ab initio simulation package (VASP)²² with the Perdew-Burke-Enzerhof (PBE) exchange-correlation functional²³ and the projector augmented wave method.²⁴ The Kohn-Sham wavefunctions were expanded using a plane wave basis set with plane wave energy cutoff of 520-530 eV. Monkhorst-Pack k-point sampling of the first Brillouin zone was adjusted to the size of slab supercells of $ZnO(10\overline{10})$, $TiO_2(110)$, and $Ga_2O_3(\overline{201})$ to ensure convergence of total energies to the number of significant figures shown. 25 Geometry optimization was carried out until the forces on all atoms dropped below a threshold of 0.01 eV Å⁻¹. The climbing image nudged elastic band (NEB) method²⁶ yielded activation barriers, with ionic coordinates relaxed until the residual force fell below 0.1 eV Å⁻¹. The spring constant was set to -5 eV Å $^{-1}$. Prior publications have detailed other specifications for surface models of ZnO⁶ and TiO₂; the same procedures were employed here.

For β -Ga₂O₃, the computed bulk lattice constants were 12.5, 3.1, and 5.8 Å in the monoclinic structure. Figure S1 shows atomic geometries in the bulk (a) and on the surface (b), along with conventional atom labeling conventions. These values lie close to the published computational²⁷ and experimental²⁸ work. The PBE band gap was 2.57 eV, which falls well below the corresponding experimental value of 4.9 eV.²⁸ However, such underestimation is well-known for the PBE method, and the present result lies close to that from another PBE work.²⁹ For O_i defect formation and bulk hopping, we used a $1 \times 4 \times 2$ supercell including 160 atoms (64 Ga atoms and 96 O atoms). The bulk hopping barrier along the $Ga_2O_3(\overline{2}01)$ direction from a bulk calculation (periodic boundary conditions in all three spatial dimensions) was 0.82 eV. For surface models, the cleaved $(\overline{201})$ termination was based upon that used in ref 29. The slab dimensions were set to 12.4 and 9.0 Å for the (2×2) plane and 18.0 Å for the depth. The vacuum space was set to 20 Å to minimize artificial interactions arising from periodic boundaries. To allow for charging of O_i that forms O_i^{2-} in the $Ga_2O_3(\overline{2}01)$ slab, we placed two Si atoms as shallow donors on the backside of the slab because the use of Vo, as in a previous work,5 yielded a deep electronic state originating from the wider band gap for Ga₂O₃. We fixed the two backmost layers, including the Si donors, and relaxed all other atomic coordinates. This procedure avoided complications due to artificial relaxations of the Si atoms.

For O_i-H_i complexes in ZnO and TiO $_2$ calculations employed the PBE + U method (Dudarev method) 30 for 3d electron corrections to the metallic elements in both ZnO ($U_{\rm eff}=6$) and TiO $_2$ ($U_{\rm eff}=5$). Other publications have detailed specifications of our supercell models for ZnO 6 and TiO $_2$. 31 To confirm the method's reliability, defect energies and ionization levels for O_i-H_i in ZnO and TiO $_2$ were compared to that of HSE06. At the same chemical potentials, PBE + U and HSE06 showed comparable defect states.

Model for Adsorption of Water on the Oxides. For all oxides, we designed 2×2 surface slabs with water and or dissociation products saturating the surfaces. For ZnO and TiO₂, adsorption geometries containing pure molecular and partially dissociated water have similar energies. We therefore investigated both possibilities in connection with O injection. For Ga_2O_3 , we found that the most stable surface state involves partial water dissociation, so we investigated only that case. For all oxides, we used a 1×2 portion of each slab to depict O injection, with the remaining 1×2 portion simply supporting molecular water and (if relevant) its dissociation products. Figures 1 and S2 illustrate the surface geometry for each

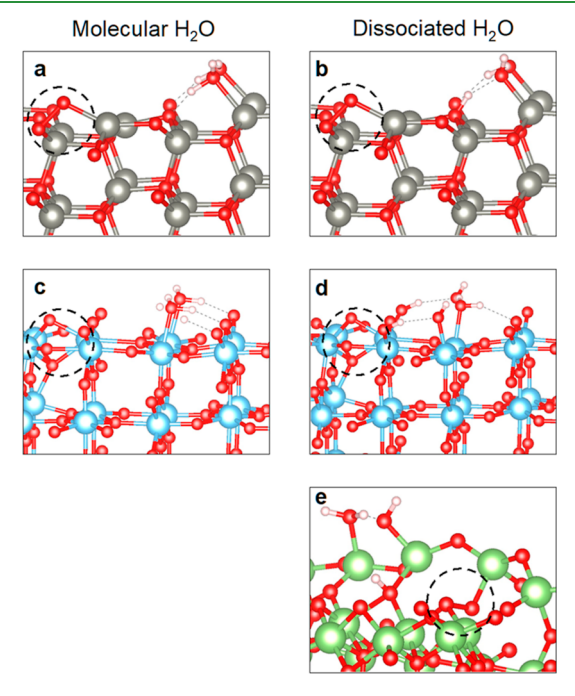


Figure 1. Adsorbate configurations for injectable O (circle) in the absence of co-adsorbed water but in the presence of co-adsorbed molecular and partially dissociated water for (a,b) $ZnO(10\overline{10})$, (c,d) $TiO_2(110)$, and (e) $Ga_2O_3(\overline{201})$ on a different row. For ZnO and Ga_2O_3 , the adsorbed O forms a neutral dumbbell structure under the experimental conditions. For TiO_2 , the structure is a surface split species charged -2.

oxide that incorporates both the portion containing injectable O and the comparatively unperturbed portion, including cases where that latter portion incorporates water that is purely molecular or partially dissociated.

Injection of O begins with an isolated O atom formed by dissociation of either $\rm H_2O$ or OH. The geometric configuration of this adsorbed, injectable O varies according to its charge state. At the Fermi energies of interest in this work, we found that adsorbed O adopts a neutral dumbbell configuration on $\rm ZnO(10\bar{1}0)^6$ and $\rm Ga_2O_3(\bar{2}01)$ and a -2 split configuration on $\rm TiO_2(110)^5$ For these configurations, periodic boundary conditions constrain the coadsorbate along a metal row to be identical on either side of the injectable O. Permutations of mixed co-adsorbates, such as $\rm H_2O$ on one side and OH on the other, require investigation of many more possibilities with much larger unit cells and were not attempted as few additional insights would be obtained.

To examine the effects of co-adsorbed water, we populated adjoining sites along the same metal rows with water or whichever decomposition products could exist stably there— H_2O , OH, or O. Energy barriers for O_i creation with these permutations were compared with each other and with no co-adsorbate at all. These calculations incorporate the effects of water only via co-adsorption and do not account explicitly for solvation effects introduced by the liquid. 32

Figures 1 and S2 show possible atomic configurations for adsorbed O for ZnO, TiO_2 , and Ga_2O_3 , focusing only on the (1×2) portion of the computational slab containing injectable O. The figure's subpanels depict injectable O with co-adsorption of H_2O , OH, and O along the same row or with no other adsorbate in that row. In particular, Figure S2a,e,i shows the injectable O co-adsorbed with molecular H_2O . Figure S2b,f,j shows the injectable O with OH. Figure S2c,g,k shows the injectable O with a second adsorbed O atom. Figure S2d,h,l shows the injectable O with no adsorbates in the same row.

Previous experimental and computational studies $^{33-36}$ agree that nonpolar ZnO and TiO₂ surfaces can support not only molecular H₂O but also its primary dissociation products OH and H. In fact, the energy difference between monolayer concentrations of adsorbed H₂O and of H₂O/OH/H mixtures falls below 0.1 eV for both ZnO(1010) and TiO₂(110). For both surfaces, we considered 1 monolayer (ML) concentrations of H₂O that is either molecular or partially dissociated. In the latter case, half the adsorbate comprises H₂O, and the other half comprises equal concentrations of OH and H. Our calculations for the molecular and partially dissociated configurations yielded energy differences of only 0.01 eV for ZnO(1010) and 0.06 eV for TiO₂(110), in alignment with the existing literature. ^{17,37,38}

We also examined various combinations of molecular and dissociated H_2O on β -Ga₂O₃($\overline{2}01$). Our calculations identified 1 ML of total adsorption as the most favorable. However, the partly dissociated form dominates, with 0.25 ML undissociated and 0.75 ML dissociated into H and OH (Figure S3). This finding aligns broadly with the existing DFT literature for water adsorption on β -Ga₂O₃($\overline{2}01$), which reports facile adsorption of both fully molecular and fully dissociated forms.²⁹ However, co-adsorbed molecular and dissociated forms were not considered.

RESULTS

Self-Diffusion Experiments. Figure 2a,c,e shows example diffusion profiles for wurtzite $ZnO(10\overline{10})$, rutile $TiO_2(110)$, and monoclinic β - $Ga_2O_3(\overline{201})$. All three surfaces are nonpolar. At the highest temperatures, ¹⁸O from the water reaches depths of up to 20 nm for ZnO and 70 nm for TiO_2 . For Ga_2O_3 , the profiles extend much deeper and lie above the natural-abundance baseline level of 0.2% everywhere within the sampled depth of 110 nm. After self-diffusion, specimens stored in air for many months at room temperature exhibit no further profile evolution. Control experiments omitting the removal of surface poisons show much less isotope penetration (Supporting Information Figure S4).

Experiments using deuterium-labeled water with natural-abundance O revealed no measurable entry of either 18 O or D into any of the oxides. The lack of excess 18 O indicates that H_2 O is the dominant source of labeled O. The lack of D implies that water dissociates completely to create adsorbed O that subsequently enters the solid.

Figure 2b,d,f shows the profiles plotted in the normalized form of eq 1 for determining key metrics including the net O_i injection flux F and the mean diffusion length λ . Figure 3 shows F and λ in the Arrhenius form for all three oxides, as well as the effective diffusivity $D_{\text{eff}} = F\lambda$. For ZnO and TiO₂, F lies mostly between 10^{11} and 10^{12} cm⁻² s⁻¹, which at the upper end is equivalent to $\sim 10^{-2}$ monolayer s⁻¹. For Ga₂O₃, the

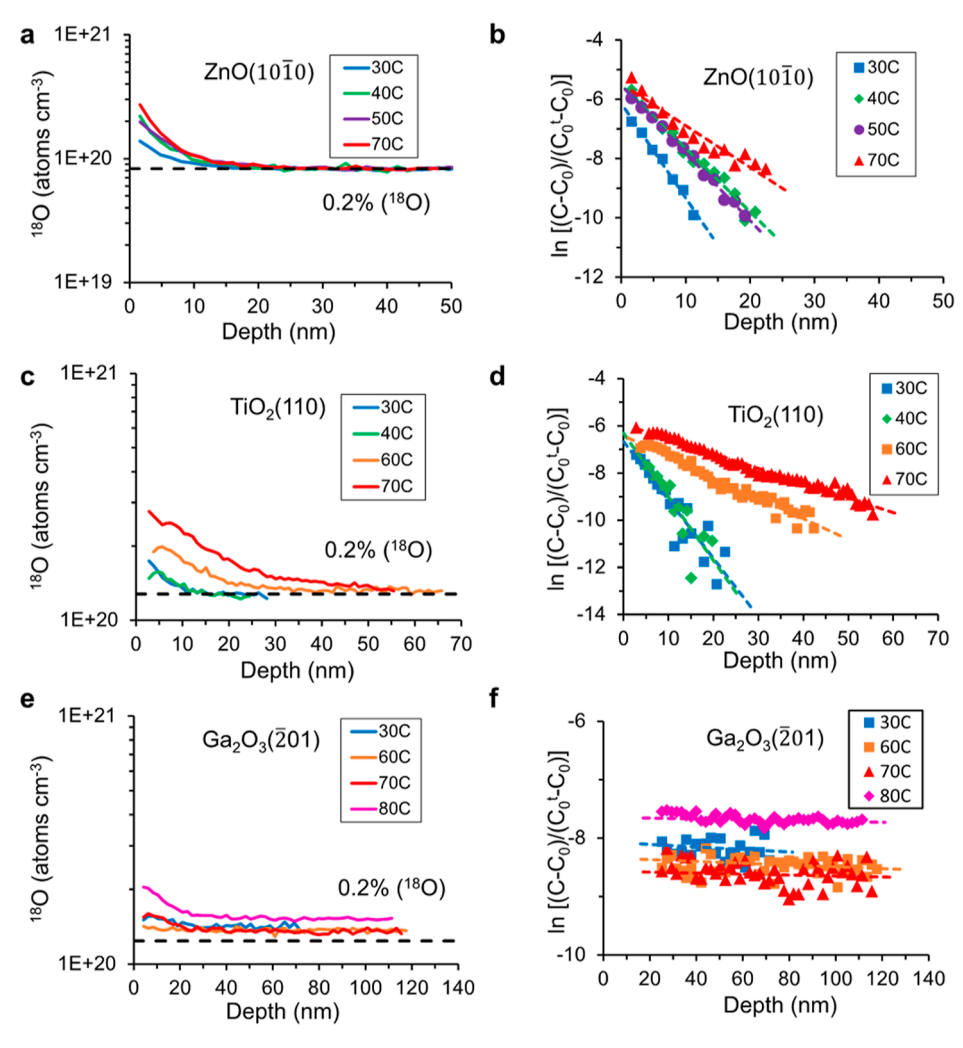


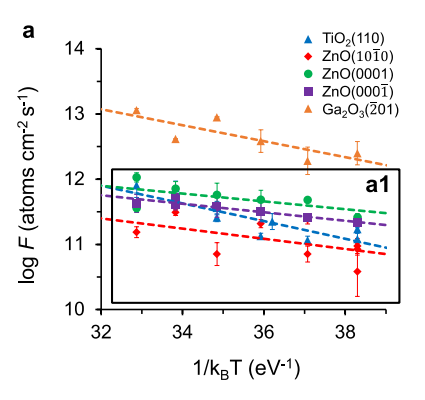
Figure 2. Example isotopic ¹⁸O concentration profiles measured for (a) $ZnO(10\overline{10})$, (c) $TiO_2(110)$, and (e) $Ga_2O_3(\overline{201})$ as a function of depth. The same profiles after normalization appear in (b), (d), and (f). Diffusion time is 1 h. The dashed lines show linear least squares fits to the normalized profiles. Ga₂O₃ profiles were fitted using points deeper than 20 nm.

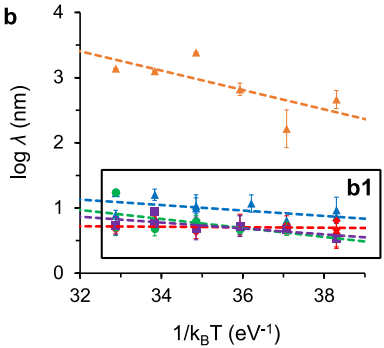
corresponding values lie about an order of magnitude higher, and λ is 2 orders of magnitude larger at 2000 nm compared to values near 9 nm for ZnO and 15 nm for TiO2. For ZnO, Figures 3 and S5 (Supporting Information) compare several crystallographic orientations of the surface, including the nonpolar (1010) and polar Zn term (0001) and O term (0001). These orientations manifest no major differences in the overall magnitude of λ and only a factor of three in F. Table 1 summarizes the activation energies for F, λ , and D_{eff} measured for all solids and crystallographic orientations examined in this work.

DFT Calculations. We employed DFT together with the climbing image NEB method²⁶ to confirm that O_i injects and diffuses readily from β -Ga₂O₃($\overline{201}$) in our temperature regime and to learn whether co-adsorption of water alters the injection barrier for any of the three oxides. The calculations focused on nonpolar crystallographic orientations, for which complicated surface reconstructions under water are the least likely. The nonpolar surfaces of all three oxides comprise long rows of metal atoms adjacent to parallel rows of O atoms. Our previous work has shown for $ZnO(10\overline{10})$ and $TiO_2(110)^{5,6}$ that in the absence of water or co-adsorbed species, O atoms adsorb in association with the metal rows. The present work (Supporting Information) indicates a similar adsorption behavior for

 $Ga_2O_3(\overline{201})$. The injection barrier is 0.86 eV, and the bulk hopping barrier is 0.82 eV. These numbers both fall below roughly 1 eV, and their ratio lies close to unity. The ratelimiting step for injection exhibits an atomic geometry close to that for site hopping. In these respects, β -Ga₂O₃($\overline{201}$) mimics the corresponding behavior for $ZnO(10\overline{10})$ and $TiO_2(110)$. For all three surfaces, co-adsorption of water in either molecular or dissociated form exerts little or no effect on the injection barrier by the most likely pathway (Table 2).

Once O_i forms at the surface and diffuses into the interior, little or no energy barrier is likely to impede mutual annihilation of O_i and V_O. However, reactions of O_i to form complexes with other point defects in oxides are possible and less understood. In particular, it is unclear whether O_i might react with hydrogen, which is ubiquitous in oxides^{39,40} as an adventitious impurity that forms complexes with other defects 40,41 including electron acceptors. 39 We therefore employed the NEB method for the example cases of O_i reacting with H_i in ZnO and TiO₂. Figure 4 shows activation barrier diagrams and corresponding atomic geometries at key points along the reaction coordinate to form the complex O_i- H_i . In ZnO, we chose an example Fermi energy (E_F) of 2.6 eV above the valence band maximum, corresponding to n-type conditions where defect formation energies indicate that O_i,





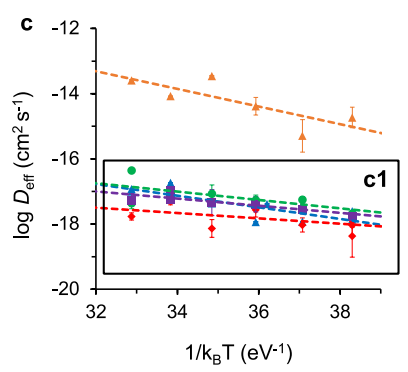


Figure 3. Arrhenius plots of (a) F, (b) λ , and (c) $D_{\rm eff}$ for various oxide surfaces. Boxes surround data points that Figure S5 (Supporting Information) also shows with an expanded vertical scale. Error bars represent standard deviations of the parameter values measured at three different places on a specimen's surface.

 H_{ij} and O_i-H_{ij} respectively, exist in charge states of 0, +1, and -1 (Figure 5). In TiO_2 , we chose $E_F=2.9$ eV where O_{ij} H_{ij} and O_i-H_{ij} respectively, exist in charge states of -2, +1, and -1 (Figure 5). The calculations revealed barriers for the association reaction of 0.2 and 0.3 eV for ZnO and TiO_2 , respectively, while the corresponding barriers for the dissociation reaction were 5.2 and 1.4 eV, respectively.

Table 2. Rate-Limiting DFT Barriers for O_i Injection with Water Co-adsorption

	activation energy (eV)						
	$ZnO(10\overline{1}0)$	TiO ₂ (110)		$Ga_2O_3(\overline{2}01)$			
neighboring adsorbate along row	dissociated H ₂ O	molecular H ₂ O	dissociated H ₂ O	dissociated H ₂ O			
H_2O	1.32	0.82	0.88	0.82			
ОН	2.01	0.82	0.88	0.82			
O	1.09	0.82	0.88	0.91			
none ^a	1.36	0.82	0.88	0.92			

^aAn artificial configuration with adsorbates present in rows adjacent to injecting O but not within the same row.

DISCUSSION

Self-diffusion involving high-temperature O_2 gas exposure is typically believed to entail near-equilibrium exchange of isotopes between the solid and fluid. The comparatively low temperatures of the present experiments are unlikely to permit such a close approach to equilibrium, especially in the O_i trapping behavior. Nevertheless, the O-rich conditions of water exposure ⁴² evidently provide a driving force sufficient for O to enter the solid, thereby leading to its slight oxidation.

A reduction reaction must exist to offset the solid's oxidation. Thermal desorption studies of H₂O from these oxide surfaces in UHV have been reported only for TiO2 and ZnO. TiO₂ shows desorption of only H₂O as the major product, even when partial dissociation occurs.²⁴ For ZnO, H₂ appears at most as a minor product. 43 Immersion in liquid water creates an environment quite different from UHV, however. Moreover, SIMS profiles show no entry of H into any of the solids, and maintaining specimen electroneutrality precludes the sustained release of H+ into the liquid. These observations suggest H2 as the most likely reduction product. No gas bubbles were observed during any of the injection experiments. However, the stoichiometry of the redox reaction, together with the observed injection rates of O, imply production rates of H2 falling at least an order of magnitude below that needed to saturate the liquid and enable the generation of visible bubbles.

The following sections discuss the likely diffusional mediator for O, trapping reactions that drive oxidation and limit penetration of O into the solid, and implications for defect engineering.

Identification of Mobile Species. Scrambling of oxygen isotopes between adsorbed water and the first layer of oxygen near room temperature is known for several oxides. ^{15,35} However, penetration of ¹⁸O further into a single-crystal solid requires a mediating defect. In ZnO, TiO₂, and many other oxides, V_O dominates the diffusive behavior of O under typical conditions with surfaces unintentionally passivated against O_i creation by ubiquitous adsorbed contaminants.

Table 1. Measured Activation Energies for F, λ , and D_{eff} of O_i

	activation energy (eV)					
	ZnO(0001)	$ZnO(000\overline{1})$	$ZnO(10\overline{10})^a$	TiO ₂ (110) ^a	$Ga_2O_3(\overline{2}01)^a$	
F	0.13 ± 0.07	0.15 ± 0.02	0.18 ± 0.10	0.31 ± 0.06	0.16 ± 0.12	
λ	0.15 ± 0.08	0.10 ± 0.04	0.01 ± 0.03	0.09 ± 0.05	0.17 ± 0.11	
$D_{ m eff}$	0.29 ± 0.14	0.25 ± 0.06	0.18 ± 0.12	0.40 ± 0.09	0.33 ± 0.12	

^aNonpolar surface.

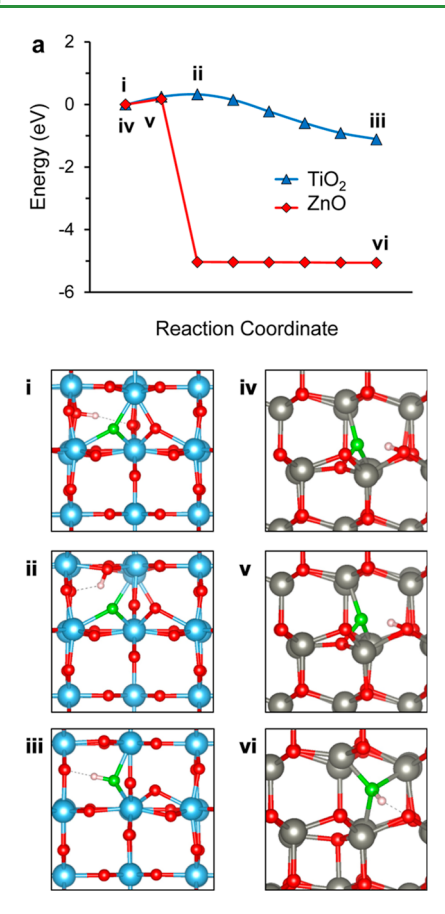


Figure 4. Activation barrier diagrams (a) with corresponding geometries (i-vi) at key points along the reaction coordinate for the reaction between O_i and H_i in bulk TiO₂ and ZnO. Rightward movement along the reaction coordinate corresponds to the association of Oi and Hi; leftward movement corresponds to the dissociation of the complex. In (i–iii) for TiO_2 ($E_F = 2.9$ eV), blue and red spheres designate titanium and lattice oxygen atoms, respectively. In (iv-vi) for ZnO ($E_{\rm F}$ = 2.6 eV), gray and red spheres designate zinc and lattice oxygen atoms, respectively. For both oxides, green spheres designate key participating O atoms, and small white spheres designate H atoms. For both oxides, the H atom remains in the formal +1 charge state throughout the association process. For TiO₂, the O atom remains in the formal -2 state. For ZnO, however, the O atom remains neutral through the transition state (v) and then absorbs two electrons from the solid to become formally (-2) while formation of the complex moves to completion.

However, poison-free TiO2 and ZnO exposed to O2 gas at 500-800 °C exhibit diffusion mediation by O₁, 3,5-7 based on evidence from several sources. First-principles computations by DFT indicate that O_i has lower formation energies and hopping barriers than V_O under O-rich conditions.^{5,4 $\overline{4}$ -46} The empirically measured activation energies for self-diffusion lie far below those for mediation by Vo, and the diffusivities are orders of magnitude higher.^{3,7} The O_i hopping barriers and injection barriers from DFT calculations agree with those from experimentally based microkinetic models of self-diffusion.⁵ For ZnO, crystal color changes add to the evidence for O_i.

Several related arguments can be made for the three oxides examined here. O_i formation energies remain lower than those for V_O, with water supplying the needed O-rich conditions.⁴² Although no microkinetic models were developed for the present work and penetration depths were too shallow to manifest crystal color changes, Vo may be excluded through

transport arguments based on mean square displacement, the onset temperature where diffusion becomes observable and the values of the effective diffusivities. The following paragraphs detail these arguments.

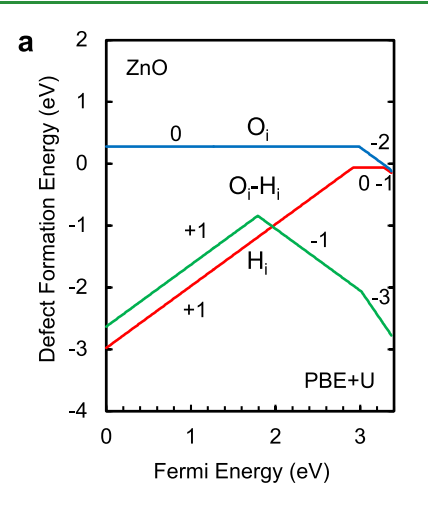
Barrier heights for hopping of O_i versus V_O for these oxides (Supporting Information Table S1) enable the experimental observation of O_i-mediated diffusion near room temperature but preclude it for V_O. An estimate for observability in SIMS comes from the random-walk mean squared displacement x^2 during time t with hopping diffusivity D_{hop} , which obeys $x^2 =$ $6D_{\text{hop}}t$. Among the oxides considered here, the lowest hopping barrier for V_O (averaged from the literature for each oxide) is 1.15 eV for TiO₂, with respective values of 1.2 and 1.5 eV for Ga₂O₃ and ZnO. The highest for O_i is 0.95 eV for ZnO, with respective values of 0.47 and 0.72 eV for Ga₂O₃ and TiO₂. We assume a hopping pre-exponential factor of 0.01 cm²/s for both O_i and V_O. 47 Estimates of the mean squared displacement using the lowest barrier for V_O and the highest barrier for O_i deliberately biases the estimates in favor of V_O. Nevertheless, the expression for mean squared displacement at 30 °C leads to x = 7 nm for O_i but only 0.2 nm for V_O . The latter value is too small for SIMS to detect. However, the observed diffusion lengths of 5 nm are close to the displacement predicted for O_i. These estimates therefore point emphatically to O_i as the more likely mediator.

Published annealing temperatures at which self-diffusion mediated by V_O becomes readily observable also argue against its participation here. Published compilations report that minimum temperatures for the onset of diffusion mediated by V_O lie near 850 °C for ZnO, 7600 °C for TiO₂, 3 and 800 °C for Ga₂O₃⁴⁶—all vastly exceeding the temperatures used here.

Examination of the effective diffusivity $D_{\rm eff}$ for $V_{\rm O}$ -mediated self-diffusion in ZnO and TiO₂ complements this approach. D_{eff} incorporates interactions of V_{O} with other defects³ and requires extrapolation down to 30-80 °C based on published values for the empirically measured activation energies. Figure 6 shows that such extrapolation yields values of $D_{\rm eff}$ lying many orders of magnitude below those observed here, even after accounting for experimental uncertainties in the high-temperature results.

The oxides exhibit diverse creation mechanisms for O_i at the surface, with notable variations in both defect charging and rate-determining step. Nevertheless, all mechanisms share the important feature that the configuration of injectable oxygen resembles a distorted analogue of bulk O_i. Moreover, the ratelimiting steps for O_i creation involve geometries that vary only modestly from the corresponding steps for bulk hopping and have barriers only slightly larger (<0.2 eV). Importantly, neither H₂O nor its dissociation products appreciably change the adsorption configurations of atomic O.

O_i Trapping. Solid-state reactions between O_i and various traps limit the depth to which O_i can penetrate the solid. V_O contributes to this trapping in the present experiments as V_O exists at the outset, and the reaction is likely to have little to no energy barrier. By contrast, trapping by Vo plays no role in selfdiffusion measurements with clean surfaces at high temperatures because the usual pre-annealing steps in O₂ remove V_O via the reaction with O_i. Native⁴⁸ or extrinsic⁴⁹ point defects and extended defects⁶ may play trapping roles that depend upon the oxide's identity and fabrication history. The computed barriers for O_i-H_i formation and dissociation suggest that this complex can play a role in the present experiments. Complexation of Oi has been considered



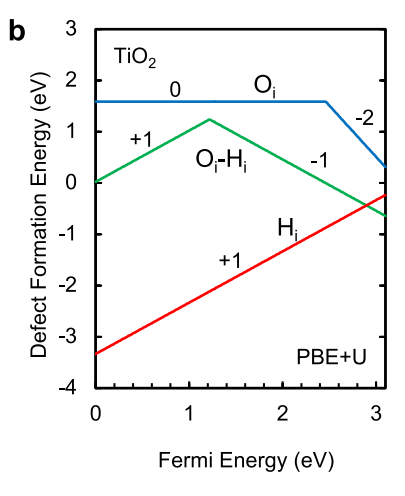
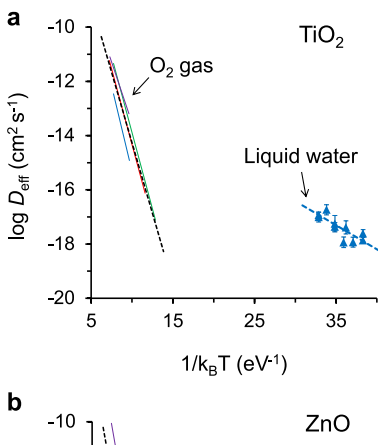


Figure 5. Defect formation energies in ZnO and TiO₂. (a) and (b), respectively, show in ZnO and TiO₂ the defect formation energy for O_i (blue), H_i (red), and the O_i – H_i defect complex (green) at 50 °C and 1 atm. Integer labels correspond to the charge of the dominant charge states.



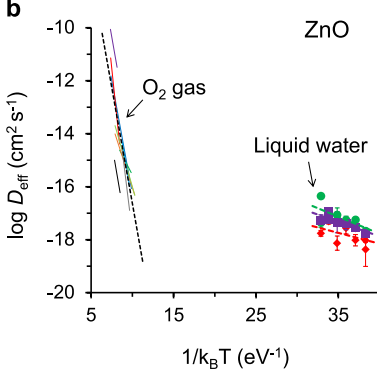


Figure 6. Comparison of $D_{\rm eff}$ between O_2 gas and liquid water. $D_{\rm eff}$ computed from the $^{18}{\rm O}$ diffusion profiles measured for (a) ${\rm TiO_2(110)}$ and (b) ${\rm ZnO(10\bar{1}0)}$, ${\rm ZnO(0001)}$, and ${\rm ZnO(000\bar{1})}$. Blue triangles, red diamonds, green circles, and purple squares, respectively, correspond to ${\rm TiO_2(110)}$, ${\rm ZnO(10\bar{1}0)}$, ${\rm ZnO(0001)}$, and ${\rm ZnO(000\bar{1})}$. Data under ${\rm O_2}$ for ${\rm TiO_2}$ were adapted from refs 62–636465 and for ZnO from refs 66–67686970. Dashed lines represent composite averages for the gas data, with average activation energies of 4.0 eV for ${\rm ZnO}^7$ and 2.4 eV for ${\rm TiO_2}$. 3 $D_{\rm eff}$ extrapolated to 30–80 °C lies many orders of magnitude below the liquid values, falling well below the horizontal axes.

previously only in niche oxide systems such as UO_2^{50} wherein the metal cation and O anion have comparable sizes. The forward barriers shown in the Results section are low enough for association to occur readily at the experimental temperatures, while the reverse barriers are high enough to prevent dissociation of O_i — H_i .

In general, formation energies for charged defects vary with $E_{\rm F}$. Figure 5 shows the charge states of $O_{\rm i}$, $H_{\rm i}$, and $O_{\rm i}-H_{\rm i}$ as a function of E_F in both ZnO and TiO₂. When the initial or final states involve charged species, the forward or reverse barriers will respectively change with $E_{\rm F}$ due to changes in the formation energies. Band gaps of semiconducting oxides widen considerably as the temperature drops from typical annealing temperatures to room temperature, and the chemical potential of oxygen changes as well due to heat capacity effects. The windows in E_F over which various charge states are stable widen or narrow accordingly. For example, comparison of the formation energy diagrams for O_i in Figure 5 and ref 31 shows that the window for neutral O_i in TiO₂ becomes much wider as the temperature decreases. For trapping sites that contribute appreciably to the carrier concentration, the reaction with injected O_i as it diffuses in will induce spatial and temporal variations in E_F . A full exposition of such a behavior lies beyond the scope of this paper, even for a single trap such as H_i. However, the DFT results suffice to suggest important kinetic roles for such traps, both for interpreting self-diffusion profiles and for defect engineering more generally.

In the present work, O_i penetration depths extend to 2 μ m in Ga_2O_3 but only 10–15 nm in ZnO and TiO₂. The penetration depths in the latter two cases lie far below the corresponding 1–10 μ m depths observed above 500 °C.^{3,5–7} It remains indeterminate at this stage whether higher temperatures serve to dissociate complexes having modest energies or instead cause those traps to diffuse out of the solid.

Prospects for Increasing Injection Rates and Penetration Depths. F equals the mathematical difference between the rates of O_i creation and annihilation. DFT activation barriers for nonpolar surfaces that create O_i are 1.19 eV for ZnO_i^6 0.82 eV for TiO_2^5 and 0.86 eV for Ga_2O_3 (this work) and appear little-affected by co-adsorption of water. These barriers substantially exceed the measured activation energies for F of 0.15–0.3 eV. Since DFT calculations have proven capable of matching injection barriers from experimentally derived mesoscale models, 5,6 the observed mismatch between injection barriers derived from DFT and the activation energies for F suggest that kinetic steps upstream of O_i injection limit the observed rates.

It follows that the rate-limiting steps act to limit the concentration of adsorbed O. Generation of adsorbed O entails complete deprotonation of water. As mentioned earlier,

dissociation of water into H and OH occurs readily on most oxides, implying that the rate-limiting step for injection involves removal of the second hydrogen. Use of the liquid state opens the way toward accomplishing this purpose through variation of pH to accelerate complete deprotonation, or application of electrochemical potentials. Such approaches are not readily available to common techniques for defect manipulation, 51-53 which rely upon introduction of foreign elements or mechanical strain during synthesis, optimization of temperature trajectory during or after synthesis, or hightemperature exposure to gases.

Increases in the injection rate may indirectly serve to increase the penetration depth as well. Sufficiently fast injection could saturate the traps so that increasing F also increases λ . Saturation would presumably begin near the surface and progress deeper over time.

Implications for Defect Engineering. Injection of O_i at modest temperatures from liquids opens new technological horizons. Oi injection could aid in the compensation of extrinsic defects, especially those that act as electron donors⁴¹ such as H, as we have seen. The reaction with V_O could also be beneficial as Vo influences material properties such as electrical conductivity, ⁵⁴ ferromagnetism, ⁵⁵ superconductivity, ⁵⁶ charge carrier lifetimes, ⁵⁷ and chemical reactivity. ⁵⁷ V_O forms readily during synthesis or heating ⁵⁸ at highly variable concentrations of the state of trations⁵⁹ that depend sensitively upon fabrication history.⁶ Methods abound to foster V_O formation,⁵⁷ but many applications would benefit from V_O elimination or fine-tuning, including photocatalysis, ⁵⁷ photoelectrochemistry, ⁵⁷ renewable energy production and storage,⁵⁷ and advanced electronics. 55,60 Diminishment of V_O typically employs exposure to oxidizing gases at high temperatures that enable not only helpful V_O diffusion to the surface but also harmful solid-state side reactions that form undesirable but thermodynamically stable defects.⁶¹ Injection of O_i by immersion in water could remove unwanted VO with kinetics that circumvent defectgenerating side reactions. Use of O_i for these purposes is best suited to solid geometries having surfaces nearby, including nanoparticles, porous oxides, and thin films.

CONCLUSIONS

We have shown that poison-free oxide surfaces inject O_i when contacted with liquid water near room temperature. For singlecrystal oxides of zinc, titanium, and gallium, Oi penetrates to depths ranging between 20 nm and 2 μ m. Such surprisingly low temperature accesses a regime wherein equilibrium concentrations of native defects become vanishingly small, and kinetic rather than thermodynamic effects dominate the defect behavior. The possibilities for wielding such kinetic tools for defect manipulation near room temperature have not been recognized. Despite variations in the mechanistic details of injection among the three oxides examined, in all cases, Oi creation requires (1) removal of ubiquitous monolayer-level surface poisons and (2) breakage of strong bonds between adsorbed O atoms and anything other than the surface. This commonality arises because the atomic geometries and energy barriers of O_i injection resemble those for bulk site hopping. This O_i almost certainly eliminates V_O within the penetration depth and may form complexes with hydrogen interstitials (H_i) that neutralize their action as adventitious donors. Such postsynthesis regulation of V_O and other defects by injected O_i would be most suited for use in nanoparticles, porous oxides,

and thin films for possible applications in electronics, energy storage, photocatalysis, and photoelectrochemistry.

ASSOCIATED CONTENT

Supporting Information

The Supporting Information is available free of charge at https://pubs.acs.org/doi/10.1021/acsami.2c07672.

> Geometric configurations of β -Ga₂O₃; close-up configurations of injectable O with co-adsorbed water; details of simulations for O_i creation; geometric configurations for key steps in O_i creation from Ga₂O₃(201) with adsorbed water; details of simulations for O_i-H_i complex formation in ZnO and TiO2; 18O profiles with and without wet etching; magnified versions of the boxed Arrhenius plots shown in Figure 3.; DFTcomputed barrier heights for hopping of O_i and V_O in ZnO, TiO₂, and Ga₂O₃; and site-to-site hopping barriers for O_i in various oxides (PDF)

AUTHOR INFORMATION

Corresponding Author

Edmund G. Seebauer – Department of Chemical and Biomolecular Engineering, University of Illinois at Urbana-Champaign, Urbana, Illinois 61801, United States; orcid.org/0000-0002-4722-3901; Email: eseebaue@ illinois.edu

Authors

Heonjae Jeong - Department of Mechanical Science and Engineering, University of Illinois at Urbana-Champaign, Urbana, Illinois 61801, United States; o orcid.org/0000-0003-4452-049X

Elif Ertekin - Department of Mechanical Science and Engineering, University of Illinois at Urbana-Champaign, Urbana, Illinois 61801, United States; oorcid.org/0000-0002-7816-1803

Complete contact information is available at: https://pubs.acs.org/10.1021/acsami.2c07672

Notes

The authors declare no competing financial interest.

ACKNOWLEDGMENTS

We thank Dr. Michael A. Scarpulla and Arkka Bhattacharyya (both of the University of Utah) for providing the Ga₂O₃. SIMS measurements were performed in the Materials Research Laboratory Central Research Facilities, University of Illinois at Urbana-Champaign. Computational resources were provided by the Illinois Campus Cluster Program in conjunction with the National Center for Supercomputing Applications, with financial support from the University of Illinois at Urbana-Champaign. This work was supported by the U.S. National Science Foundation under grant DMR 17-09327. For the computational work involving Ga₂O₃, E.E. acknowledges partial support from the Air Force Office of Scientific Research under award FA9550-21-0078.

REFERENCES

(1) Chason, E.; Picraux, S. T.; Poate, J. M.; Borland, J. O.; Current, M. I.; Diaz de la Rubia, T.; Eaglesham, D. J.; Holland, O. W.; Law, M. E.; Magee, C. W.; Mayer, J. W.; Melngailis, J.; Tasch, A. F. Ion Beams

- in Silicon Processing and Characterization. J. Appl. Phys. 1997, 81, 6513-6561.
- (2) McCarty, K. F.; Nobel, J. A.; Bartelt, N. C. Vacancies in Solids and the Stability of Surface Morphology. *Nature* **2001**, *412*, 622–625.
- (3) Hollister, A. G.; Gorai, P.; Seebauer, E. G. Surface-Based Manipulation of Point Defects in Rutile TiO2. *Appl. Phys. Lett.* **2013**, *102*, 231601.
- (4) Li, M.; Seebauer, E. G. Surface-Based Control of Oxygen Interstitial Injection into ZnO via Submonolayer Sulfur Adsorption. *J. Phys. Chem. C* **2016**, *120*, 23675–23682.
- (5) Jeong, H.; Ertekin, E.; Seebauer, E. G. Kinetic Control of Oxygen Interstitial Interaction with TiO2(110) via the Surface Fermi Energy. *Langmuir* **2020**, *36*, 12632–12648.
- (6) Jeong, H.; Li, M.; Kuang, J.; Ertekin, E.; Seebauer, E. G. Mechanism of Creation and Destruction of Oxygen Interstitial Atoms by Nonpolar Zinc Oxide(10-10) Surfaces. *Phys. Chem. Chem. Phys.* **2021**, 23, 16423–16435.
- (7) Gorai, P.; Ertekin, E.; Seebauer, E. G. Surface-Assisted Defect Engineering of Point Defects in ZnO. *Appl. Phys. Lett.* **2016**, *108*, 241603.
- (8) Bowker, M.; Bennett, R. A. The Role of Ti3+ Interstitials in TiO2 (110) Reduction and Oxidation. *J. Phys.: Condens. Matter* **2009**, 21, 474224.
- (9) Mulheran, P. A.; Nolan, M.; Browne, C. S.; Basham, M.; Sanville, E.; Bennett, R. A. Surface and Interstitial Ti Diffusion at the Rutile TiO2(110) Surface. *Phys. Chem. Chem. Phys.* **2010**, *12*, 9763–9771.
- (10) Gilliard-AbdulAziz, K. L.; Seebauer, E. G. Microkinetic Model for Reaction and Diffusion of Titanium Interstitial Atoms near a TiO2 (110) Surface. *Phys. Chem. Chem. Phys.* **2018**, 20, 4587–4596.
- (11) Van Orman, J. A.; Crispin, K. L. Diffusion in Oxides. Rev. Mineral. Geochem. 2010, 72, 757–825.
- (12) Spurgeon, S. R.; Sassi, M.; Ophus, C.; Stubbs, J. E.; Ilton, E. S.; Buck, E. C. Nanoscale Oxygen Defect Gradients in UO2+x Surfaces. *Proc. Natl. Acad. Sci.* **2019**, *116*, 17181–17186.
- (13) Wang, M.; Debernardi, A.; Berencén, Y.; Heller, R.; Xu, C.; Yuan, Y.; Xie, Y.; Böttger, R.; Rebohle, L.; Skorupa, W.; Helm, M.; Prucnal, S.; Zhou, S. Breaking the Doping Limit in Silicon by Deep Impurities. *Phys. Rev. Appl.* **2019**, *11*, 54039.
- (14) Calvin, J. J.; Rosen, P. F.; Ross, N. L.; Navrotsky, A.; Woodfield, B. F. Review of Surface Water Interactions with Metal Oxide Nanoparticles. *J. Mater. Res.* **2019**, *34*, 416–427.
- (15) Jakub, Z.; Meier, M.; Kraushofer, F.; Balajka, J.; Pavelec, J.; Schmid, M.; Franchini, C.; Diebold, U.; Parkinson, G. S. Rapid Oxygen Exchange between Hematite and Water Vapor. *Nat. Commun.* **2021**, *12*, 6488.
- (16) Wang, Y.; Muhler, M.; Wöll, C. Spectroscopic Evidence for the Partial Dissociation of H2O on ZnO(10-10). *Phys. Chem. Chem. Phys.* **2006**, *8*, 1521–1524.
- (17) Diebold, U. Perspective: A Controversial Benchmark System for Water-Oxide Interfaces: H2O/TiO2 (110). *J. Chem. Phys.* **2017**, 147, 040901.
- (18) Kilner, J. A.; Steele, B. C. H.; Ilkov, L. Oxygen Self-Diffusion Studies Using Negative-Ion Secondary Ion Mass Spectrometry (SIMS). *Solid State Ionics* **1984**, *12*, 89–97.
- (19) Gorai, P.; Hollister, A. G.; Seebauer, E. G. Measurement of Defect-Mediated Oxygen Self-Diffusion in Metal Oxides. *ECS J. Solid State Sci. Technol.* **2012**, *1*, Q21–Q24.
- (20) Gorai, P.; Seebauer, E. G. Kinetic Model for Electric-Field Induced Point Defect Redistribution near Semiconductor Surfaces. *Appl. Phys. Lett.* **2014**, *105*, 021604.
- (21) Swallow, J. E. N.; Varley, J. B.; Jones, L. A. H.; Gibbon, J. T.; Piper, L. F. J.; Dhanak, V. R.; Veal, T. D. Transition from Electron Accumulation to Depletion at β -Ga2O3 Surfaces: The Role of Hydrogen and the Charge Neutrality Level. *APL Mater.* **2019**, 7, 022528.
- (22) Kresse, G.; Furthmüller, J. Efficient Iterative Schemes for Ab Initio Total-Energy Calculations Using a Plane-Wave Basis Set. *Phys. Rev. B: Condens. Matter Mater. Phys.* **1996**, *54*, 11169–11186.

- (23) Perdew, J. P.; Burke, K.; Ernzerhof, M. Generalized Gradient Approximation Made Simple. *Phys. Rev. Lett.* **1996**, *77*, 3865–3868.
- (24) Kresse, G.; Joubert, D. From Ultrasoft Pseudopotentials to the Projector Augmented-Wave Method. *Phys. Rev. B: Condens. Matter Mater. Phys.* 1999, 59, 1758–1775.
- (25) Monkhorst, H. J.; Pack, J. D. Special Points for Brillouin-Zone Integrations. *Phys. Rev. B: Solid State* **1976**, *13*, 5188.
- (26) Henkelman, G.; Uberuaga, B. P.; Jónsson, H. A Climbing Image Nudged Elastic Band Method for Finding Saddle Points and Minimum Energy Paths. *J. Chem. Phys.* **2000**, *113*, 9901–9904.
- (27) Varley, J. B.; Weber, J. R.; Janotti, A.; Van de Walle, C. G. Oxygen Vacancies and Donor Impurities in β -Ga2O3. *Appl. Phys. Lett.* **2010**, *97*, 142106.
- (28) Geller, S. Crystal Structure of B-Ga2O3. J. Chem. Phys. 1960, 33, 676-684.
- (29) Anvari, R.; Spagnoli, D.; Parish, G.; Nener, B. Density Functional Theory Simulations of Water Adsorption and Activation on the (-201) β -Ga2O3 Surface. *Chem.—Eur. J.* **2018**, *24*, 7445–7455.
- (30) Dudarev, S. L.; Botton, G. A.; Savrasov, S. Y.; Humphreys, C. J.; Sutton, A. P. Electron-Energy-Loss Spectra and the Structural Stability of Nickel Oxide: An LSDA+ U Study. *Phys. Rev. B: Condens. Matter Mater. Phys.* 1998, 57, 1505.
- (31) Jeong, H.; Seebauer, E. G.; Ertekin, E. First-Principles Description of Oxygen Self-Diffusion in Rutile TiO2: Assessment of Uncertainties Due to Enthalpy and Entropy Contributions. *Phys. Chem. Chem. Phys.* **2018**, *20*, 17448–17457.
- (32) Mathew, K.; Sundararaman, R.; Letchworth-Weaver, K.; Arias, T. A.; Hennig, R. G. Implicit Solvation Model for Density-Functional Study of Nanocrystal Surfaces and Reaction Pathways. *J. Chem. Phys.* **2014**, *140*, 84106.
- (33) Calzolari, A.; Catellani, A. Water Adsorption on Nonpolar ZnO (1010) Surface: A Microscopic Understanding. *J. Phys. Chem. C* **2009**, 113, 2896–2902.
- (34) Ma, C.; Jin, W.; Ma, X.; Han, H.; Yu, J.; Wu, Y. Water Adsorption Behaviors of High Index Polar Surfaces in ZnO. *Appl. Surf. Sci.* **2019**, 498, 143898.
- (35) Henderson, M. A. Structural Sensitivity in the Dissociation of Water on TiO2 Single-Crystal Surfaces. *Langmuir* **1996**, *12*, 5093–5098.
- (36) Di Valentin, C.; Tilocca, A.; Selloni, A.; Beck, T. J.; Klust, A.; Batzill, M.; Losovyj, Y.; Diebold, U. Adsorption of Water on Reconstructed Rutile TiO2(011)-(2×1): TiO Double Bonds and Surface Reactivity. *J. Am. Chem. Soc.* **2005**, *127*, 9895–9903.
- (37) Meyer, B.; Rabaa, H.; Marx, D. Water Adsorption on ZnO(10-10): From Single Molecules to Partially Dissociated Monolayers. *Phys. Chem. Chem. Phys.* **2006**, *8*, 1513–1520.
- (38) Wang, Z. T.; Wang, Y. G.; Mu, R.; Yoon, Y.; Dahal, A.; Schenter, G. K.; Glezakou, V. A.; Rousseau, R.; Lyubinetsky, I.; Dohnálek, Z. Probing Equilibrium of Molecular and Deprotonated Water on TiO2(110). *Proc. Natl. Acad. Sci. U.S.A.* **2017**, *114*, 1801–1805.
- (39) McCluskey, M. D.; Tarun, M. C.; Teklemichael, S. T. Hydrogen in Oxide Semiconductors. *J. Mater. Res.* **2012**, 27, 2190–2198.
- (40) Li, H.; Robertson, J. Behaviour of Hydrogen in Wide Band Gap Oxides. J. Appl. Phys. 2014, 115, 203708.
- (41) Ingebrigtsen, M. E.; Kuznetsov, A. Y.; Svensson, B. G.; Alfieri, G.; Mihaila, A.; Badstübner, U.; Perron, A.; Vines, L.; Varley, J. B. Impact of Proton Irradiation on Conductivity and Deep Level Defects in β -Ga2O3. *APL Mater.* **2019**, *7*, 022510.
- (42) Kowalski, P. M.; Meyer, B.; Marx, D. Composition, Structure, and Stability of the Rutile TiO2 (110) Surface: Oxygen Depletion, Hydroxylation, Hydrogen Migration, and Water Adsorption. *Phys. Rev. B: Condens. Matter Mater. Phys.* **2009**, *79*, 115410.
- (43) Xie, R.; Sekiguchi, T.; Ishigaki, T.; Ohashi, N.; Li, D.; Yang, D.; Liu, B.; Bando, Y. Enhancement and Patterning of Ultraviolet Emission in ZnO with an Electron Beam. *Appl. Phys. Lett.* **2006**, *88*, 134103.

- (44) Janotti, A.; Van de Walle, C. G. Native Point Defects in ZnO. Phys. Rev. B 2007, 76, 165202.
- (45) Lee, H.-Y.; Robertson, J. Doping and Compensation in Nb-Doped Anatase and Rutile TiO2. J. Appl. Phys. 2013, 113, 213706.
- (46) Kyrtsos, A.; Matsubara, M.; Bellotti, E. Migration Mechanisms and Diffusion Barriers of Vacancies in Ga2O3. Phys. Rev. B 2017, 95, 245202.
- (47) Shaw, D. Atomic Diffusion in Semiconductors; Springer Science & Business Media, 2012.
- (48) Yu, J.; Bai, X.-M.; El-Azab, A.; Allen, T. R. Oxygen Transport in Off-Stoichiometric Uranium Dioxide Mediated by Defect Clustering Dynamics. J. Chem. Phys. 2015, 142, 094705.
- (49) Hou, Q.; Buckeridge, J.; Lazauskas, T.; Mora-Fonz, D.; Sokol, A. A.; Woodley, S. M.; Catlow, C. R. A. Defect Formation in In2O3 and SnO2: A New Atomistic Approach Based on Accurate Lattice Energies. J. Mater. Chem. C 2018, 6, 12386-12395.
- (50) Flitcroft, J. M.; Molinari, M.; Brincat, N. A.; Williams, N. R.; Storr, M. T.; Allen, G. C.; Parker, S. C. The Critical Role of Hydrogen on the Stability of Oxy-Hydroxyl Defect Clusters in Uranium Oxide. J. Mater. Chem. A 2018, 6, 11362-11369.
- (51) Canino, M.; Regula, G.; Xu, M.; Ntzoenzok, E.; Pichaud, B. Defect Engineering via Ion Implantation to Control B Diffusion in Si. Mater. Sci. Eng. B 2009, 159-160, 338-341.
- (52) Tuller, H. L.; Bishop, S. R. Point Defects in Oxides: Tailoring Materials Through Defect Engineering. Annu. Rev. Mater. Res. 2011, 41, 369-398.
- (53) Park, J. S.; Kim, S.; Xie, Z.; Walsh, A. Point Defect Engineering in Thin-Film Solar Cells. Nat. Rev. Mater. 2018, 3, 194-210.
- (54) McCluskey, M. D. Point Defects in Ga2O3. J. Appl. Phys. 2020,
- (55) Zhang, Y.; Cui, Z.; Zhu, L.; Zhao, Z.; Liu, H.; Wu, Q.; Wang, J.; Huang, H.; Fu, Z.; Lu, Y. Negative Effect of Oxygen Vacancies on Ferromagnetism in Ru-Doped BaSnO3 Materials. Appl. Phys. Lett. 2020, 117, 052406.
- (56) Kang, H. J.; Dai, P.; Campbell, B. J.; Chupas, P. J.; Rosenkranz, S.; Lee, P. L.; Huang, Q.; Li, S.; Komiya, S.; Ando, Y. Microscopic Annealing Process and Its Impact on Superconductivity in T'-Structure Electron-Doped Copper Oxides. Nat. Mater. 2007, 6, 224-229.
- (57) Zu, D.; Wang, H.; Lin, S.; Ou, G.; Wei, H.; Sun, S.; Wu, H. Oxygen-Deficient Metal Oxides: Synthesis Routes and Applications in Energy and Environment. Nano Res. 2019, 12, 2150-2163.
- (58) Pinto, F. M.; Suzuki, V. Y.; Silva, R. C.; La Porta, F. A. Oxygen Defects and Surface Chemistry of Reducible Oxides. Front. Mater. 2019, 6, 260.
- (59) Gunkel, F.; Christensen, D. V.; Chen, Y. Z.; Pryds, N. Oxygen Vacancies: The (in) Visible Friend of Oxide Electronics. Appl. Phys. Lett. 2020, 116, 120505.
- (60) Wu, X.; Migas, D. B.; Li, X.; Bosman, M.; Raghavan, N.; Borisenko, V. E.; Pey, K. L. Role of Oxygen Vacancies in HfO2-Based Gate Stack Breakdown. Appl. Phys. Lett. 2010, 96, 172901.
- (61) Schmidt-Mende, L.; MacManus-Driscoll, J. L. ZnO-Nanostructures, Defects, and Devices. Mater. Today 2007, 10, 40-48.
- (62) Haul, R.; Dümbgen, G. Sauerstoff-Selbstdiffusion in Rutilkristallen. J. Phys. Chem. Solids 1965, 26, 1-10.
- (63) Lee, D.-K.; Yoo, H.-I. Unusual Oxygen Re-Equilibration Kinetics of TiO2 $-\delta$. Solid State Ionics **2006**, 177, 1-9.
- (64) Derry, D. J.; Lees, D. G.; Calvert, J. M. A Study of Oxygen Self-Diffusion in the C-Direction of Rutile Using a Nuclear Technique. J. Phys. Chem. Solids 1981, 42, 57-64.
- (65) Arita, M.; Hosoya, M.; Kobayashi, M.; Someno, M. Depth Profile Measurement by Secondary Ion Mass Spectrometry for Determining the Tracer Diffusivity of Oxygen in Rutile. J. Am. Ceram. Soc. 1979, 62, 443-446.
- (66) Moore, W. J.; Williams, E. L., II. Diffusion of Zinc and Oxygen in Zinc Oxide. Discuss. Faraday Soc. 1959, 28, 86-93.
- (67) Robin, R.; Cooper, A. R.; Heuer, A. H. Application of a Nondestructive Single-spectrum Proton Activation Technique to

- Study Oxygen Diffusion in Zinc Oxide. J. Appl. Phys. 1973, 44, 3770-
- (68) Hoffman, J. W.; Lauder, I. Diffusion of Oxygen in Single Crystal Zinc Oxide. Trans. Faraday Soc. 1970, 66, 2346-2353.
- (69) Tomlins, G. W.; Routbort, J. L.; Mason, T. O. Oxygen Diffusion in Single-crystal Zinc Oxide. J. Am. Ceram. Soc. 1998, 81, 869-876.
- (70) Haneda, H.; Sakaguchi, I.; Watanabe, A.; Ishigaki, T.; Tanaka, J. Oxygen Diffusion in Single-and Poly-Crystalline Zinc Oxides. J. Electroceram. 1999, 4, 41-48.

□ Recommended by ACS

In Situ Tuning of Defects and Phase Transition in Titanium Dioxide by Lithiothermic Reduction

Chao Wang, Zhenda Lu, et al.

IANITARY 08 2020

ACS APPLIED MATERIALS & INTERFACES

READ 2

Atomic Scale Characterization of Fluxional Cation Behavior on Nanoparticle Surfaces: Probing Oxygen Vacancy Creation/Annihilation at Surface Sites

Ethan L. Lawrence, Peter A. Crozier, et al.

JANUARY 28, 2021

ACS NANO

READ **C**

Effect of Surface Nanostructures and Speciation on **Undercooling for Low-Temperature Solder Alloys**

Andrew Martin, Martin Thuo, et al.

FEBRUARY 24, 2022

ACS APPLIED NANO MATERIALS

RFAD 17

Oxidation of Gallium-based Liquid Metal Alloys by Water

Megan A. Creighton, Christopher E. Tabor, et al.

OCTOBER 22, 2020

LANGMUIR

READ **C**

Get More Suggestions >